Capacitive Aptasensor Coupled with Microfluidic Enrichment for Real-Time Detection of Trace SARS-CoV-2 Nucleocapsid Protein

Haochen Qi,[#] Zhiwen Hu,[#] Zhongliang Yang, Jian Zhang,* Jie Jayne Wu,* Cheng Cheng, Chunchang Wang, and Lei Zheng*

Read Online

ACCESS | Metrics & More | Article Recommendations | Supporting Information

ABSTRACT: The pandemic caused by severe acute respiratory syndrome coronavirus 2 (SARS-CoV-2) has lasted for almost 2 years. Stemming its spread has posed severe challenges for clinical virus detection. A long turnaround time, complicated operation, and low accuracy have become bottlenecks in developing detection techniques. Adopting a direct antigen detection strategy, we developed a fast-responding and quantitative capacitive aptasensor for ultratrace nucleocapsid protein detection based on a low-cost microelectrode array (MEA) chip. Employing the solid–liquid interface capacitance with a sensitivity of picofarad level, the tiny change on the MEA surface can be definitively detected. As a result, the limit of detection reaches an ultralow level of femtogram per milliliter in different matrices. Integrated with efficient microfluidic enrichment, the response time of this sensor from the sample to the result is shortened to 15 s, completely meeting the real-time detection demand. Moreover, the wide linear range of the sensor is from 10^{-5} to 10^{-2} ng/mL, and a high selectivity of 6369:1 is achieved. After application and evaluation in different environmental and body fluid matrices, this sensor and the detection method have proved to be a label-free, real-time, easy-to-operate, and specific strategy for SARS-CoV-2 screening and diagnosis.
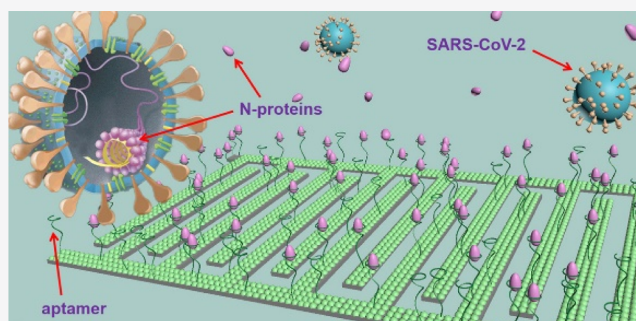
INTRODUCTION

Beginning in December 2019, a series of serious pneumonia cases were reported.[1] Named as COVID-19, this infectious disease has struck most countries in the world, infecting more than 220 million individuals and killing more than 2.7 million to date.[2] COVID-19 is still uncontrollable and has become the most serious global plague in this century. Similar to all the other pandemics, pathogen determination is the first and vital step for clinical diagnosis. Therefore, rapid, accurate, and specific detection of severe acute respiratory syndrome coronavirus 2 (SARS-CoV-2) and its biomarkers is urgently needed.[3,4]

To date, the dominant technique in clinical practice for SARS-CoV-2 detection is polymerase chain reaction (PCR)-based nucleic acid testing (NAT).[5−7] When NATs are performed, complicated operations are necessary, such as cycles of amplification and reverse transcription, leading to a test time of at least several hours.[8] Nonetheless, a number of false-negative results from NATs have been reported, with an estimated accuracy of only 30−50% for laboratory-confirmed COVID-19 cases.[9] Another multicenter U.S. study has demonstrated that the accuracy rate of NATs can be as low as 82%, even for symptomatic patients.[10] Unsurprisingly, it has been verified that the number of real infected cases in the U.S. is much greater than the number of cases NATs can diagnose.[7]

In fact, false negatives from initial PCR tests may occur up to 54% of the time when virus concentrations are not high in the upper respiratory tracts of the virus carriers.[11] In addition, around 10−30% of infectors are found to be asymptomatic carriers,[12] and infectiousness can peak before symptom onset.[13] Therefore, recognition of SARS-CoV-2 at low concentrations needs to be greatly improved. To improve the reliability of laboratory diagnosis, SARS-CoV-2-specific antibody detection is often used as an auxiliary means to NATs. It is known that various types of antibodies always appear after viral antigens become present in the infected bodies. As a result, the accuracy of antibody-dependent diagnosis is not good (about 40%), even within 7 days of symptom onset.[14,15] Therefore, antibody detection is not reliable enough, especially in the beginning of the disease course.

To overcome the technological limitations in COVID-19 screening and diagnosis, emerging technologies have also been

reported, such as CRISPR-based methods with a shorter turnaround time of 40 min,[16] but complicated genetic sequencing is still necessary for these methods. To realize a nonsequencing diagnosis, strategies of protein antigen detection have gained increasing attention due to their simple detection mechanisms.[6,17,18] Nucleocapsid (N-) protein is a structural protein that helps perform viral RNA replication, assembly, and release.[19] It is much more abundant in the human body than virion itself, even at the beginning of infection. More importantly, N-protein has been verified to be much more stable during virus mutation[20] and more abundant compared with spike protein, another important antigen in SARS-CoV-2 diagnosis.[21] Therefore, N-protein is regarded as a good biomarker for early SARS-CoV-2 infection[22] and variant infection diagnosis.[6,20−22]

For specific detection of N-protein, the common probes for target recognition are antibodies[23−25] and aptamers.[26−28] Antibodies are traditional probes applied for immune recognition, but the costs of screening, production, and preservation are much higher than those of chemical synthetic aptamers. With advantages on molecular stability, adjustable affinity, and batch consistency, aptamers are more suitable for developing low-cost sensors for large-scale applications.[28,29] To date, immunoassays for N-protein are mostly reported due to the availability of antibodies,[24,25,30−32] although it is encouraging that researchers have recently focused on aptasensor development.[27,33] Based on the traditional sensing methods, such as ELISA and electrochemistry, the lowest limit of detection (LOD) of the abovementioned assays is 6.25 pg/mL.[32] At the same time, the shortest turnaround time is not satisfied (about 1 h) due to the lack of efficient techniques for target enrichment.[25]

Based on a microelectrode array (MEA) chip modified with a specific aptamer, we developed a microfluidics-coupled capacitive sensor for trace N-protein detection in both phosphate-buffered saline (PBS) and practical samples. The conceptual illustration of the sensor, the measurement system, and N-protein capturing is shown in Figure 1. Utilizing the solid−liquid interface capacitance as an ultrasensitive indicator,
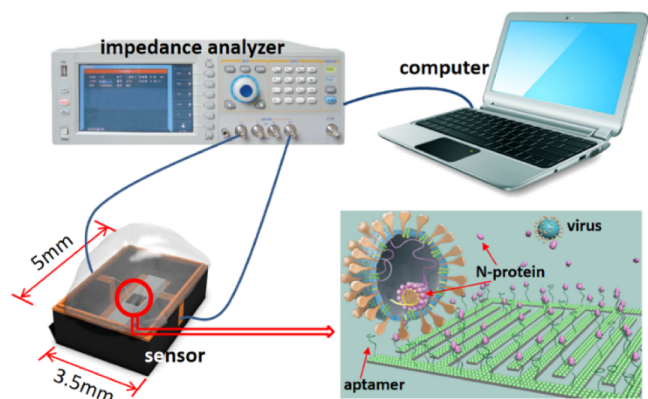

Figure 1. Conceptual illustration of the sensor, measurement system, and N-protein capturing. The sensor is prepared based on an MEA chip modified with the aptamer. The impedance analyzer provides an AC signal for stimulating microfluidic enrichment and also measures the capacitance change from the sensor. Trace N-protein as a biomarker from SARS-CoV-2 is recognized and captured by the aptamer. Interface capacitance sensing coupled with the microfluidic effect enables real-time and sensitive detection.

low LODs of femtogram per milliliter levels are achieved in different matrices. Simultaneously, target enrichment is realized via microfluidic effects during the capacitance test process, leading to an extremely short response time of 15 s. Also, a wide linear range from 10^{-5} to 10^{-2} ng/mL is achieved. This aptasensor and its detection method provide a competitive solution for real-time and low-cost screening and diagnosis of SARS-CoV-2.

■ EXPERIMENTAL SECTION

Reagents and Samples. An aptamer for SARS-CoV-2 N-protein with a sequence of GCT GGA TGT CGC TTA CGA CAA TAT TCC TTA GGG GCA CCG CTA CAT TGA CAC ATC CAG C[28] and a scrambled single-stranded nucleic acid of TCG CGC GAG TCG TCT GGG GAC AGG GAG TGC GCT GCT CCC CCC GCA TCG TCC TCC C were synthesized by Sangon Biotech (Shanghai) Co., Ltd., China, both being 5′-amino modified. The platelet-derived growth factor (PDGF)-BB and histone (HT) of the calf thymus were also ordered from Sangon. The recombinant N-protein (purity: >95%) expressed by the prokaryotic system with the host of *Escherichia coli* was provided by Cellregen Life Science Technology Co., Ltd., China. The corresponding sodium dodecyl sulfate-polyacrylamide gel electrophoresis (SDS-PAGE) result of this protein is presented in Figure S1. The recombinant spike protein (SP) was also bought from CellReGen. The peptidoglycan (PGN) was purchased from Nanjing Duly Biotechnology Co., Ltd., China. The human immunoglobulin G (IgG) and albumin (AB) were purchased from Hefei Bomei Biotechnology Co. Ltd., China. The pooled human serum and plasma were bought from Guangzhou Hongquan Biological Technology Co., Ltd., China. The saliva for sensor recalibration was pooled using samples from three healthy volunteers without respiratory or oral infection. The blocker of 6-mercapto-1-hexanol (6-MCH) was bought from Aladdin Biotechnology Co., Ltd., China. The aptamer and 6-MCH were both diluted in 0.05× PBS with concentrations of 2.5 μM and 1 mM, respectively.

The N-protein and six interferences (PGN, PDGF-BB, IgG, AB, SP, and HT) diluted in 0.1× PBS had a series of concentrations with a 10-fold increase from 10^{-5} to 10^{-2} ng/mL. The tap water was 1:1 diluted in 0.2× PBS to make the conductivity close to 0.1× PBS, and this medium was used to obtain the following spiked samples in tap water. The serum, plasma, saliva, and the tap water were all first spiked with N-protein to obtain an initial concentration of 10 ng/mL. Then, these samples were centrifuged at 2000 rpm for 5 min and diluted with 0.1× PBS to obtain the N-protein concentration from 10^{-5} to 10^{-2} ng/mL. The corresponding six backgrounds were prepared using the blank matrices, which are 1:1000 diluted with 0.1× PBS.

Nine throat swab-collected saliva samples were from the above three volunteers, and every volunteer had samples collected from them three times on different days. The volume of each saliva sample was about 0.1 mL. After collection, the swabs were dripped with a 1 μL N-protein solution of 10 ng/mL in 0.1× PBS to simulate positive clinical samples. These swabs were then soaked in 0.1× PBS of 1 mL for 5 min; the theoretical maximum of N-protein concentration in this solution was around 10^{-3} ng/mL. The negative group was prepared using a similar protocol without adding N-protein.

Capacitive Sensing. When an electrode is immersed in an electrolyte solution, charges will accumulate on its surface, and
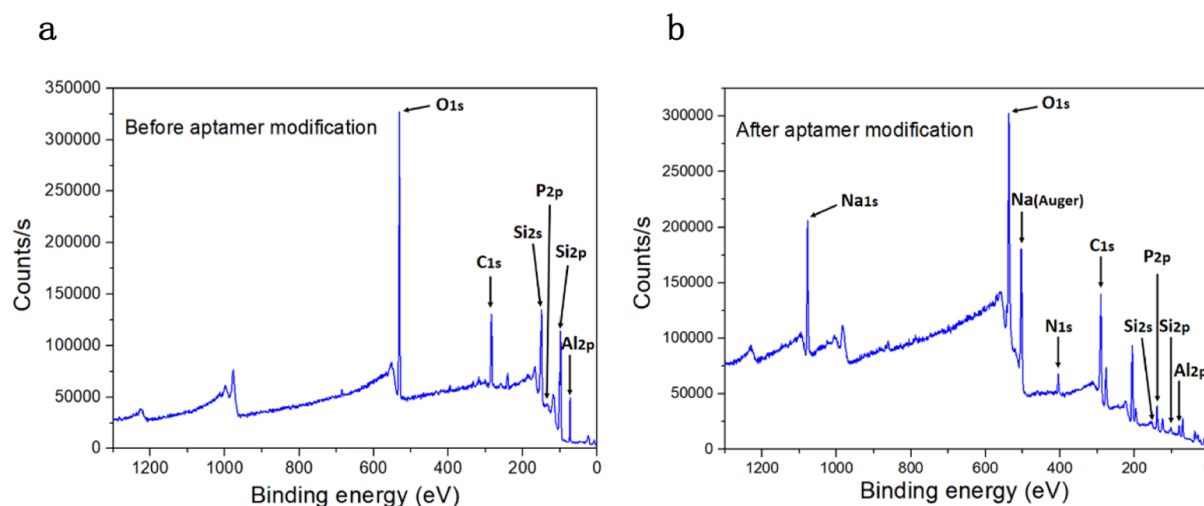
a

b

Figure 2. XPS survey spectrums for the MEA surface characterization. (a) Spectrum on an electrode surface before aptamer modification. (b) Spectrum on an electrode surface after aptamer modification.

the counter-ion layer is then induced near the surface. An interface capacitance is formed by a so-called electric double layer (EDL) due to the separation of charges at the interface between the electrode and the electrolyte.[34] This solid−liquid system is equivalent to a circuit, and the total capacitance is composed of the bulk and interface capacitance. Because the bulk capacitance from the whole solution remains stable, the output capacitance is only affected by the change from interface capacitance. According to previous investigations, the interface capacitance at the picofarad level can work as an ultrasensitive indicator of trace adsorption on the electrode surface.[35,36] In this work, the MEA chip is functionalized by the aptamer and blocker as shown in Figure S2, where the thickness of the total dielectric layer is composed of EDL and the self-assembled aptamer layer. When N-protein particles are captured by the aptamer, the interface dielectric layer will become thicker, and the interface capacitance will become smaller as deduced in eq S1 in the Supporting Information.

It is characteristic of electrolytic capacitors to yield slightly different capacitance values even when measuring the same device at different times. Considering that the sensing process produces only a few percentages of change, this small variation could lead to uncertainty in the detection results if the absolute capacitance is used. An optimal strategy to eliminate this variation is to utilize the change of capacitance normalized by its initial value. In this work, the change rate of normalized capacitance is defined as an indicator of N-protein adsorption in a detection duration.

Microfluidic Enrichment of N-Protein. For rapid detection of trace analytes, efficient target concentration or sedimentation remains a great challenge. In the past decade, the strengths of microfluidics for target enrichment have been shown.[34,37,38] Owing to the simple and single device without pumps and microchannels, alternating-current electrokinetic (ACEK) effects are competitive for manipulating and enriching nanoparticles in dozens of seconds.[39−41] Among the three ACEK effects of AC electro-osmosis (ACEO), AC electro-thermal (ACET), and dielectrophoretic (DEP) forces,[42] DEP force has been demonstrated to be dominant when the targets are as large as proteins.[37] As DEP force is proportional to the particle radius to the third power[37,41,43] and the radii of proteins are at least 10 times larger than those of common

ions, the applied force on the N-proteins can be at least 1000 times greater than on ions in the same solution. DEP force is expressed in eq S2 in the Supporting Information, in which it is also determined by the electric field strength. As a result, the applied voltage is an important parameter determining DEP force on the N-protein particles.

Sensor Preparation and Test Procedure. In this work, the MEA chips were commercially supplied (AVX Corps' KYOCERA 418K), which are commonly used as surface acoustic wave (SAW) crystal oscillators. The MEA chip, measuring 5 × 3.5 × 1.5 mm in size, was packaged in a rectangular ceramic chamber covered with a cap, as shown in Figure S3a. After removing the cap, the aluminized electrode array on the base as shown in Figure S3b could be functionalized. The sensor preparation is described as follows: (1) the MEA chip was soaked in acetone for 15 min, rinsed with isopropanol for 10 s, rinsed with DI water for 10 s, and dried with an air gun; (2) the chip was treated with ultraviolet light for 20 min to increase the surface hydrophilicity; (3) the aptamer (2.5 μM, 10 μL) was dropped into the chamber; (4) 5 h later, 6-MCH (1 mM, 10 μL) was added, and the chip was blocked for 3.5 h; (5) the chip was washed with 0.1× PBS for N-protein detection. To verify the capability of target recognition, two types of dummy sensors were prepared for control experiments. One was the MEA chips modified with the nonspecific single-stranded DNA, and the other was the MEA chips without any aptamer or DNA. Both types were blocked in the same way as the functionalized sensors so as to keep a similar surface topography as the functionalized ones.

For sensor preparation, the aptamer was first modified with a (−NH₂) group at its 5′ end. After incubation, the aptamer could self-assemble on the aluminum MEA surface through the binding force between (−NH₂) and aluminum. Here, the binding force mainly has two mechanisms: chelation and electrostatic adsorption. The (−NH₂) group with lone pair electrons can coordinate with most metals providing vacant orbits, so the aptamer links with aluminum through chelation. Because the neutral solution of 0.1× PBS is not so conducive to amino protonation, the electrostatic adsorption might be weaker than coordinate. For 6-MCH, it can bind to the MEA surface via Al−S bonds by means of ligand exchange, similar to the chelation between (−NH₂) and aluminum. Meanwhile,
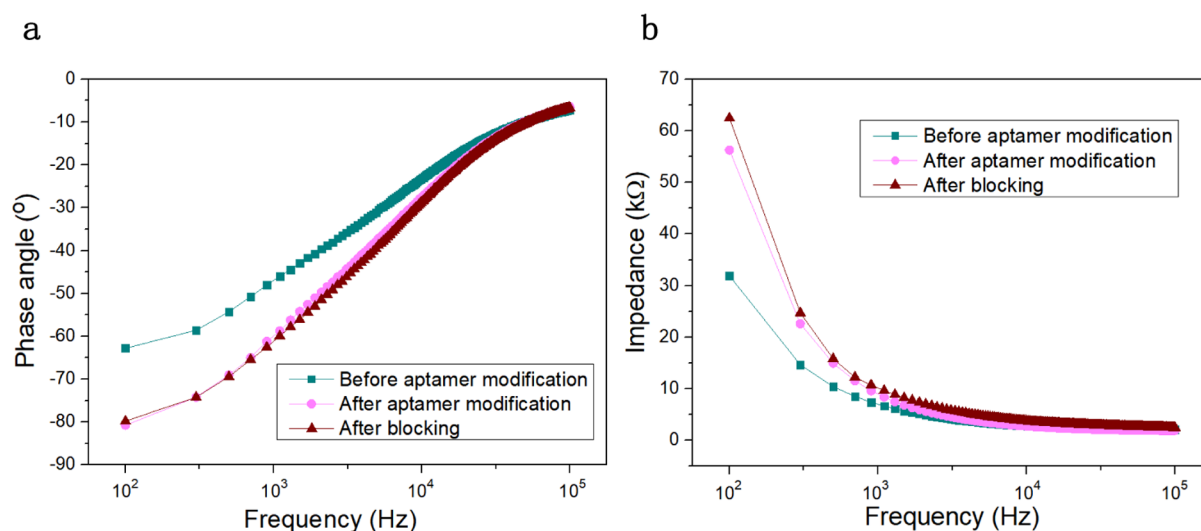
Figure 3. Bode plots for electrode surface characterization. (a) Phase angle spectrums and (b) impedance spectrums of the electrode−solution system from 100 to 10^5 Hz.

there should also be some physical adsorption during both aptamer and blocker modification via van der Waals' force.

After the aptasensor was prepared, 10 μL of the analyte was added into the chamber. The sensor was then connected to an impedance analyzer (Tonghui, TH2829.C) in the parallel measuring mode as shown in Figure 1. An AC signal of 100 mV and 100 kHz was applied to MEA when the capacitance was continuously recorded within dozens of seconds and the change rate of normalized capacitance as the response was subsequently calculated. Every sensor was used once, and every concentration for analysis was tested three times to obtain an average response unless specifically stated. For body fluid samples, all detection should be finished in 2 h at room temperature after the samples are prepared. Otherwise, non-negligible microbial growth might affect detection. Using dummy sensors, the sample test procedure was the same.

Test Condition Determination. To realize a successful N-protein detection, frequency and voltage are the two key parameters of the applied AC signal. According to previous research, 100 kHz is a suitable frequency for this type of SAW chip to maximize the DEP force. Under this frequency, the DEP force has been verified as positive toward the electrode surface.[29,37,44] To regulate the DEP force for N-protein particles, the applied voltage as a key parameter for testing should be optimized before detection. According to the positive correlation between the voltage and electric field, a higher voltage will contribute to stronger DEP force, while an excessively high voltage may lead to premature saturation of adsorption and even nonspecific adsorption. Therefore, a proper voltage is needed to make a significant response but inhibit adsorption saturation. The voltage optimization is shown in Figure S4 in the Supporting Information, deciding the applied root-mean-square (RMS) AC voltage of 100 mV for N-protein detection.

■ RESULTS AND DISCUSSION

Characterization of Functionalized MEA. The aptasensor was developed based on an MEA chip after aptamer and blocker modification. X-ray photoelectron spectroscopy (XPS) and electrical tests were performed for the characterization of surface coverage by probe molecules. Figure 2a,b shows the

XPS survey spectrums obtained on an MEA surface before and after aptamer modification, respectively. In Figure 2a, the element of aluminum (Al 2p) as the electrode surface material is clearly observed before functionalization. However, aluminum can hardly be found in Figure 2b after aptamer modification, indicating a good coverage by the aptamer. Rather than carbon (C 1s) and oxygen (O 1s), the element of nitrogen (N 1s) as a characteristic organic element should only be from the aptamer in Figure 2b. There should also be some residual elements from the PBS in which the aptamer was diluted. For example, sodium (Na 1s), chlorine (Cl 2p), and phosphorus (P 2p) are accordant with the characteristic peaks from Na_2HPO_4 and NaCl, the components of PBS. In Figure 2, two main lines of silicon (Si 2p and Si 2s) are denoted, which are considered to be from silicon dioxide of the quartz substrate. Their significantly reduced peaks after aptamer modification indicate the existence of the aptamer layer on the substrate. In conclusion, the XPS spectra demonstrate a successful surface functionalization by the aptamer.

As an effective electrical method to describe the change on electrodes, Bode plots from 100 to 10^5 Hz are presented in Figure 3. As shown in Figure 3a, there is a significant hysteresis on the phase angle spectrum after the aptamer is immobilized on the electrode surface, which is considered to be caused by the thicker dielectric layer with the aptamer than a single EDL above the electrode surface. After blocking, the phase angle does not change anymore because the dielectric layer does not become thicker, although it is patched with smaller blocker molecules at the sites among the aptamer molecules. As shown in Figure 3b, the impedance modulus becomes significantly larger after aptamer immobilization, which is especially noticeable at low frequencies. This clearly indicates the lower conductivity of the solid−liquid system due to the coated nonconducting aptamer layer. After blocking, the impedance modulus changes little, similar to the trend of phase angle. In conclusion, both the changes of phase angle and impedance indicate a good modification by the aptamer and blocker on the electrode surface.

Dose Response and Sensor Calibration. The transient normalized capacitance from target N-protein in 0.1× PBS was first acquired for performance evaluation for this sensor. A
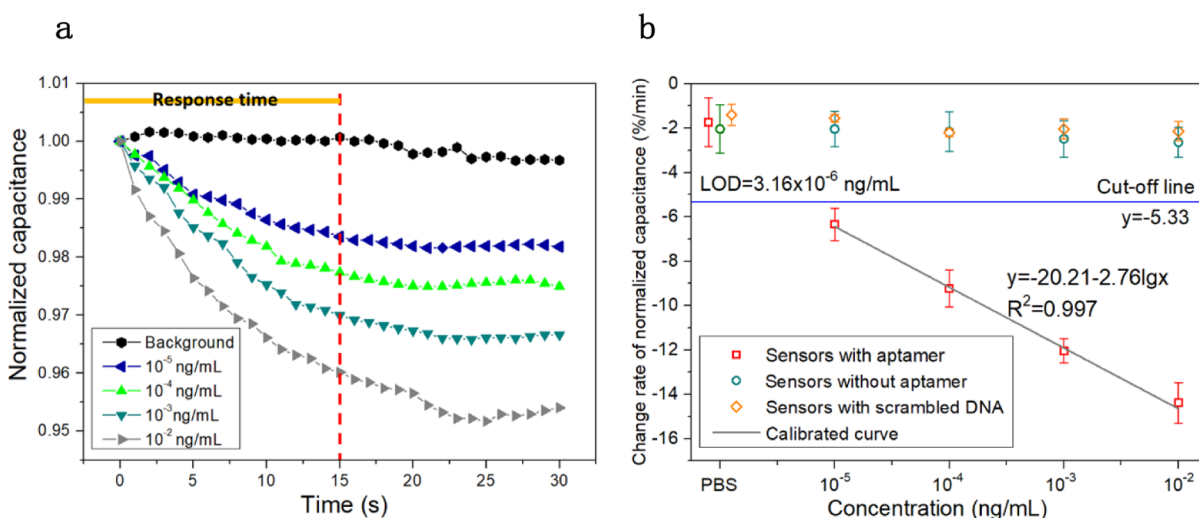
Figure 4. Dose response (10^{-2} to 10^{-5} ng/mL) from N-protein in 0.1× PBS. (a) Transient curves obtained in 30 s. The transient capacitance normalized by its initial value at 0 s was continuously measured. (b) Sensor calibration. The red symbols represent the response from the functionalized sensors (with the aptamer), and the green and orange symbols are from dummy ones (without the aptamer or with scrambled DNA), respectively. Every dot is from the averaged triplicate responses, and the bars are their standard deviations (STDEVs).
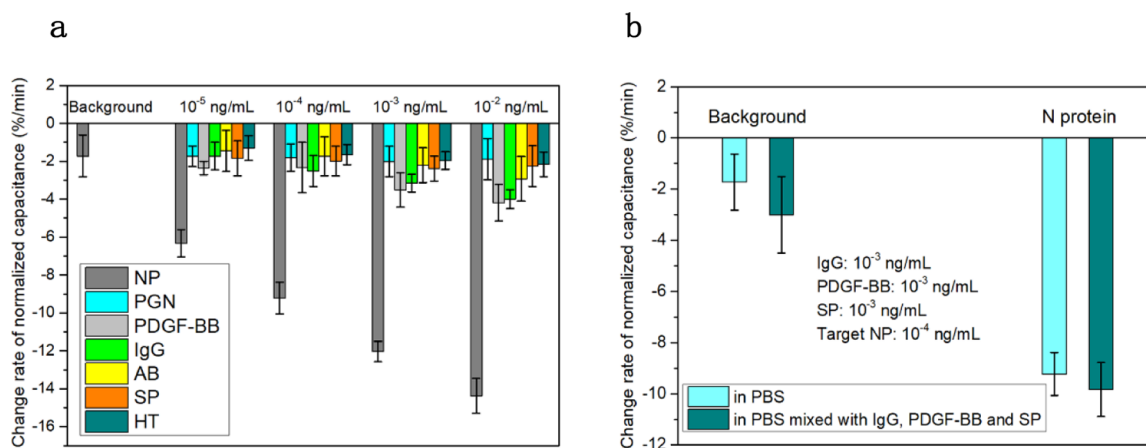

Figure 5. Selectivity tests for the aptasensor. (a) Response comparison between N-protein and six interferences. Here, the abbreviation of NP represents N-protein. The background is 0.1× PBS, and the interferences are PGN, PDGF-BB, IgG, AB, SP, and HT. The concentration of every analyte is from 10^{-5} to 10^{-2} ng/mL. (b) N-protein detection in 0.1× PBS mixed with IgG, PDGF-BB, and SP. The concentration of N-protein is 10^4 ng/mL, and the concentration of three interferences is 10 times higher. All the tests were performed in triplicate with the averaged responses and their STDEVs.

series of N-protein concentrations were tested, from 10^{-5} to 10^{-1} ng/mL, increasing by 10-fold. After an investigation of the response range, the upper limit was set to 10^{-2} ng/mL according to the adsorption saturation,[34] as shown in Figure S5 in the Supporting Information. In Figure 4a, the normalized capacitance changing with time was continuously measured in a duration of 30 s, forming a set of transient curves with different slopes. We observed that the curves flattened after around 10 s, and too long a duration did not yield a better response resolution. To obtain a more significant readout in as short a duration as possible, we chose 15 s as the sensor's response time so as to meet the requirements of point-of-care tests.

The response is defined as the change rate of normalized capacitance (%/min), and it is exactly the slope value of the transient curve in Figure 4a. Least-square fitting was used to get these slopes in this work. Then, dose response was determined, as shown in Figure 4b, in which the negligible response from dummy sensors (without the aptamer or with

scrambled DNA) are presented to verify the aptamer's target specificity. The dose response yields a semi-log linear relationship, that is, y (%/min) = $-20.21-2.76 \lg x$ (ng/mL), with a squared Pearson correlation coefficient, R^2, of 0.997. Here, we defined a cutoff line ($y = -5.33$) by three standard deviations from the background toward the positive response (with negative values).[45] Then, the LOD of this sensor in 0.1× PBS was obtained at the intersection of the calibration curve and cutoff line, which was 3.16×10^{-6} ng/mL (3.16 fg/mL). According to the results in Figure 4b, this sensor provides a good semi-log linear dose response, and the LOD reaches an extremely low level.

Selectivity of N-Protein Detection. As a crucial figure of merit for a biosensor, the selectivity of target N-protein detection should be investigated. In this work, six interferences were tested (PGN, PDGF-BB, IgG, AB, SP, and HT) as introduced in the experimental section. The first four interferences may exist in the body fluids, and SP is another structural protein found in the SARS-CoV-2 virus. As for HT,
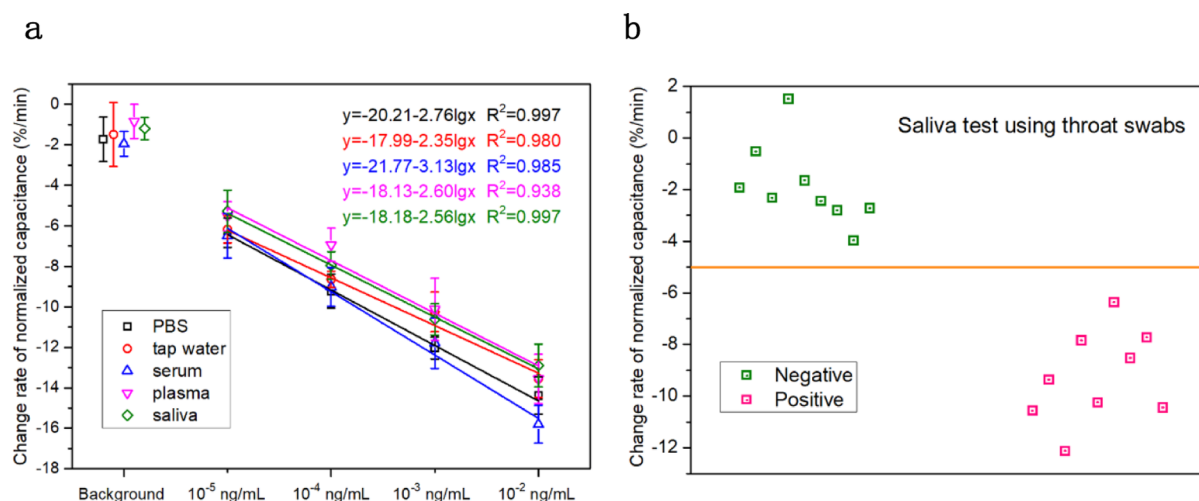
E

Figure 6. N-protein detection in practical matrices. (a) Dose response in tap water, pooled human serum, pooled human plasma, and human saliva, together with their calibrations. All tests were performed in triplicate presented with the average responses and their STDEVs. (b) Saliva test using throat swab collected samples. Two groups both of 9 samples were tested for negative and positive verification.

it is for verifying the sensor's specificity when different positively charged alkaline proteins (N-protein and HT) are tested because there is a weak natural affinity between nucleic acids and these proteins. The response comparison is shown in Figure 5a, where all the interferences produce little responses, much smaller than that of N-protein in the full range. Among the nontarget responses, the largest one of −4.19%/min is from PDGF-BB at 10^{-2} ng/mL, which equals the response from N-protein at 1.57×10^{-6} ng/mL calculated by the calibration equation. Therefore, this sensor has a high selectivity of 6369:1 (10^{-2} ng/mL: 1.57×10^{-6} ng/mL).

Because multiple interferences presented in the collected samples are common in practice, they should be considered for sensor applications. Here, we constructed a complex medium containing IgG, PDGF-BB, SP, and N-protein to investigate the sensor's performance in the presence of multiple interferences. The concentration of N-protein was 10^{-4} ng/mL, while three interferences were all 10^{-3} ng/mL. As shown in Figure 5b, although the medium with multiple interferences as the background produced a higher response than in 0.1× PBS, the positive response from N-protein was very similar to that in PBS. The reason might be related to the competitive adsorption of the target N-protein compared with the interferences. The affinity between the aptamer and N-protein should be much larger than any other particles. When there are N-protein particles, they will occupy the sites on the electrode surface with priority. Therefore, the interferences have little impact on the result. Considering the one-tenth concentration of N-protein compared with the interferences, this positive response demonstrates an excellent selectivity of the aptasensor in the presence of multiple interferences.

N-Protein Detection in Practical Matrices. For practical SARS-CoV-2 detection, environmental and clinical matrices are both of special concern. In this work, tap water, pooled serum, pooled plasma, and human saliva are used as four different practical matrices. Following the protocol introduced in the experimental section, the initial N-protein spiked matrices had a concentration of 10 ng/mL, which is a typical concentration in clinical blood samples from confirmed patients.[30] Then, the spiked samples were diluted to obtain a series of concentrations falling into the sensor's linear range.

The detection results are shown in Figure 6a, where the recalibration is performed for these dose responses. The slope of four calibration curves is from −2.35 to −3.13, and R^2 is from 0.938 to 0.997, reflecting similar response characteristics of the sensor compared with those in standard PBS. The LODs of N-protein in tap water, serum, plasma, and saliva are 9.62×10^{-6}, 1.82×10^{-6}, 2.16×10^{-6}, and 1.26×10^{-6} ng/mL, respectively, all of the same level. According to Figure 6a, the concentration in practical matrices may have a deviation of 10 times from that in standard PBS if the calibration equation in 0.1× PBS is used. Because the practical matrices for detection have been at least 1:1000 diluted using the raw samples, this deviation will not cause a wrong diagnosis in practice. Certainly, precise detection can be achieved if the corresponding equations for special matrices are adopted. In conclusion, this investigation confirms the reliability of this sensor applied with different practical matrices of both environmental and clinical samples.

Because throat swabs are mainstream tools for sample collection in SARS-CoV-2 screening and diagnosis, the sensor performance needs to be evaluated with the throat swab collection method. Here, two groups of samples were tested, and each group contained nine saliva samples collected via throat swabs. The negative group was from healthy volunteers, and the positive group was constructed by spiking N-protein into the same samples with a theoretical upper limit of concentration at 10^{-1} ng/mL. The protocol for sample collection and spike can be found in the experimental section. These two groups were used to simulate real samples from uninfected and infected individuals. Before the final test, these samples were immersed and diluted in 0.1× PBS (with a dilution factor of 1:100) to reduce the nonspecific adsorption mainly from large microorganisms. Therefore, the directly detected samples corresponded to 10^{-3} ng/mL.

In Figure 6b, the dots in the clusters were quite separated compared with the values of certain concentrations obtained from previous bodily fluid samples, reflecting a much larger standard deviation in the current test. The cause may be the inconsistent volume of samples collected by throat swabs as well as the probable inadequate dissolution of the saliva from the swabs. These factors are unavoidable when assays and

biosensors are used in practical applications, and Figure 6b illustrates their impact on the test accuracy. Even so, there are distinct response regions for the two groups in the figure, with a cutting line at the response of -5.0%. In fact, the simulated N-protein concentration of 10^{-1} ng/mL or lower in the positive swab samples was approximately $1/10-1/100$ of the threshold for SARS-CoV-2 infection confirmation. The detection result demonstrates the sensitive recognition of trace N-protein by the sensor even after a 1:100 dilution. Therefore, this sensor has a good applicability for different sample collection modes.

CONCLUSIONS

To date, the dominant techniques for SARS-CoV-2 determination are PCR-based RNA sequencing methods, which are time-consuming, complicated in operation, and costly. As an alternative, the advantages of using N-protein as a target antigen in fast and direct diagnosis of SARS-CoV-2 infection are becoming apparent. Utilizing a specific aptamer for recognizing N-protein from SARS-CoV-2, an MEA-based aptasensor has been developed by employing solid−liquid interface capacitance as a sensitive indicator. The variation of this capacitance is at the picofarad level, leading to a high resolution of the readout. As a feature, microfluidic enrichment is integrated with the capacitance acquiring process, independent of extra equipment or treatment for preconcentration. Also, because of efficient enrichment, ultralow LODs of nanograms per milliliter level are achieved in 15 s in various matrices. Another merit of this sensor is the linear range of $10^{-5}-10^{-2}$ ng/mL, which is quite wide but lower than the clinical diagnostic threshold, allowing dilution steps for subsequent detection and analysis.

Using different types of environmental and body fluid matrices, the performance of this aptasensor is validated. After high-factor dilutions, the LODs and calibrated curves are both consistent, making the sensor applicable for known or unknown matrices without recalibration. Moreover, the saliva collected by the throat swab is detected in addition to the body fluids collected by routine sampling methods. The positive group can be accurately recognized with the N-protein concentrations at around 10^{-1} ng/mL or much lower. Owing to the capability of detecting ultratrace N-protein, this sensor can be used for raw samples without culture or amplification and shows potential for screening asymptomatic carriers or individuals at the presymptomatic stage. Based on a commercial MEA chip, the cost of this sensor is controlled below 1 U.S. dollar, and the sensor can work as a disposable device. In summary, this aptasensor and the associated test strategy provide a low-cost and practical solution for label-free, nonsequencing, real-time, and large-scale screening and diagnosis of SARS-CoV-2 contamination and infection.

ASSOCIATED CONTENT

ⓈI Supporting Information

The Supporting Information is available free of charge at https://pubs.acs.org/doi/10.1021/acs.analchem.1c04296.

> Stripes from SDS-PAGE for the recombinant N-protein; schematic of the sensing mechanism based on the change of the dielectric layer; MEA chip for sensor preparation; optimization of the voltage for the test; dose response for determination of the dynamic range;

expression of normalized interface capacitance; and expression of EDP force (PDF)

AUTHOR INFORMATION

Corresponding Authors

Jian Zhang − *College of Electrical and Electronic Engineering, Wenzhou University, Wenzhou 325035, China; School of Food and Biological Engineering, Hefei University of Technology, Hefei 230009, China;* Email: jianzhang@wzu.edu.cn

Jie Jayne Wu − *Department of Electrical Engineering and Computer Science, The University of Tennessee, Knoxville, Tennessee 37996, United States;* ⓘ orcid.org/0000-0001-5143-9425; Email: jaynewu@utk.edu

Lei Zheng − *School of Food and Biological Engineering, Hefei University of Technology, Hefei 230009, China;* Email: lei.zheng@aliyun.com

Authors

Haochen Qi − *College of Electrical and Electronic Engineering, Wenzhou University, Wenzhou 325035, China*

Zhiwen Hu − *School of Computer and Information Engineering, Zhejiang Gongshang University, Hangzhou 310018, China*

Zhongliang Yang − *Department of Electronic Engineering, Tsinghua University, Beijing 100084, China*

Cheng Cheng − *Department of Engineering and Technology Management, Morehead State University, Morehead, Kentucky 40351, United States;* ⓘ orcid.org/0000-0002-5401-6185

Chunchang Wang − *Laboratory of Dielectric Functional Materials, School of Materials Physics and Engineering, Anhui University, Hefei 230601, China;* ⓘ orcid.org/0000-0002-2349-1098

Complete contact information is available at:
https://pubs.acs.org/10.1021/acs.analchem.1c04296

Author Contributions

[#]H.Q. and Z.H. contributed equally to this work. J.Z., J.J.W., and L.Z. conceived the research and supervised the project. H.Q. and J.Z. performed the experiments and analyzed the data. Z.H., Z.Y., C.C, C.W., and L.Z. provided the resource. H.Q., J.Z., and J.J.W. wrote the paper. All authors discussed the results and commented on the manuscript.

Notes

The authors declare no competing financial interest.

REFERENCES

(1) Velavan, T. P.; Meyer, C. G. *Trop. Med. Int. Health* **2020**, *25*, 278−280.

(2) Jia, H.; Zhang, A.; Yang, Y.; Cui, Y.; Xu, J.; Jiang, H.; Tao, S.; Zhang, D.; Zeng, H.; Hou, Z.; Feng, J. *Lab Chip* **2021**, *21*, 2398−2406.

(3) Iravani, S. *Mater. Adv.* **2020**, *1*, 3092−3103.

(4) Yuan, X.; Yang, C.; He, Q.; Chen, J.; Yu, D.; Li, J.; Zhai, S.; Qin, Z.; Du, K.; Chu, Z.; Qin, P. *ACS Infect. Dis.* **2020**, *6*, 1998−2016.

(5) Tsang, N. N. Y.; So, H. C.; Ng, K. Y.; Cowling, B. J.; Leung, G. M.; Ip, D. K. M. *Lancet Infect. Dis.* **2021**, *21*, 1233−1245.

(6) Carter, L. J.; Garner, L. V.; Smoot, J. W.; Li, Y.; Zhou, Q.; Saveson, C. J.; Sasso, J. M.; Gregg, A. C.; Soares, D. J.; Beskid, T. R.; Jervey, S. R.; Liu, C. *ACS Central Sci.* **2020**, *6*, 591−605.

(7) Silverman, J. D.; Hupert, N.; Washburne, A. D. *Sci. Transl. Med.* **2020**, *12*, No. eabc1126.

(8) Chu, D. K. W.; Pan, Y.; Cheng, S. M. S.; Hui, K. P. Y.; Krishnan, P.; Liu, Y.; Ng, D. Y. M.; Wan, C. K. C.; Yang, P.; Wang, Q.; Peiris, M.; Poon, L. L. M. *Clin. Chem.* **2020**, *66*, 549−555.

(9) Qiu, G.; Gai, Z.; Tao, Y.; Schmitt, J.; Kullak-Ublick, G. A.; Wang, J. *ACS Nano* **2020**, *14*, 5268−5277.

(10) Ridgway, J. P.; Pisano, J.; Landon, E.; Beavis, K. G.; Robicsek, A. *Open Forum Infect. Dis.* **2020**, *7*, ofaa315.

(11) Arevalo-Rodriguez, I.; Buitrago-Garcia, D.; Simancas-Racines, D.; Zambrano-Achig, P.; Del Campo, R.; Ciapponi, A.; Sued, O.; Martinez-García, L.; Rutjes, A. W.; Low, N.; Bossuyt, P. M.; Perez-Molina, J. A.; Zamora, J. *PLoS One* **2020**, *15*, No. e0242958.

(12) Shental, N.; Levy, S.; Wuvshet, V.; Skorniakov, S.; Shalem, B.; Ottolenghi, A.; Greenshpan, Y.; Steinberg, R.; Edri, J.; Gillis, R.; Goldhirsh, M.; Moscovici, K.; Sachren, S.; Friedman, L. M.; Nesher, L.; Shemer-Avni, Y.; Porgador, A.; Hertz, T. *Sci. Adv.* **2020**, *6*, No. eabc5961.

(13) He, X.; Lau, E. H. Y.; Wu, P.; Deng, X.; Wang, J.; Hao, X.; Lau, Y. C.; Wong, J. Y.; Guan, Y.; Tan, X.; Mo, X.; Chen, Y.; Liao, B.; Chen, W.; Hu, F.; Zhang, Q.; Zhong, M.; Wu, Y.; Zhao, L.; Zhang, F.; Cowling, B. J.; Li, F.; Leung, G. M. *Nat. Med.* **2020**, *26*, 672−675.

(14) Martinaud, C.; Hejl, C.; Igert, A.; Bigaillon, C.; Bonnet, C.; Mérens, A.; Wolf, A.; Foissaud, V.; Leparc-Goffart, I. *J. Clin. Virol.* **2020**, *130*, 104571.

(15) Zhao, J.; Yuan, Q.; Wang, H.; Liu, W.; Liao, X.; Su, Y.; Wang, X.; Yuan, J.; Li, T.; Li, J.; Qian, S.; Hong, C.; Wang, F.; Liu, Y.; Wang, Z.; He, Q.; Li, Z.; He, B.; Zhang, T.; Fu, Y.; Ge, S.; Liu, L.; Zhang, J.; Xia, N.; Zhang, Z. *Clin. Infect. Dis.* **2020**, *71*, 2027−2034.

(16) Broughton, J. P.; Deng, X.; Yu, G.; Fasching, C. L.; Servellita, V.; Singh, J.; Miao, X.; Streithorst, J. A.; Granados, A.; Sotomayor-Gonzalez, A.; Zorn, K.; Gopez, A.; Hsu, E.; Gu, W.; Miller, S.; Pan, C.-Y.; Guevara, H.; Wadford, D. A.; Chen, J. S.; Chiu, C. Y. *Nat. Biotechnol.* **2020**, *38*, 870−874.

(17) Porte, L.; Legarraga, P.; Vollrath, V.; Aguilera, X.; Munita, J. M.; Araos, R.; Pizarro, G.; Vial, P.; Iruretagoyena, M.; Dittrich, S.; Weitzel, T. *Int. J. Infect. Dis.* **2020**, *99*, 328−333.

(18) Udugama, B.; Kadhiresan, P.; Kozlowski, H. N.; Malekjahani, A.; Osborne, M.; Li, V. Y. C.; Chen, H.; Mubareka, S.; Gubbay, J. B.; Chan, W. C. W. *ACS Nano* **2020**, *14*, 3822−3835.

(19) Zeng, W.; Liu, G.; Ma, H.; Zhao, D.; Yang, Y.; Liu, M.; Mohammed, A.; Zhao, C.; Yang, Y.; Xie, J.; Ding, C.; Ma, X.; Weng, J.; Gao, Y.; He, H.; Jin, T. *Biochem. Biophys. Res. Commun.* **2020**, *527*, 618−623.

(20) Casasanta, M. A.; Jonaid, G. M.; Kaylor, L.; Luqiu, W. Y.; Solares, M. J.; Schroen, M. L.; Dearnaley, W. J.; Wilson, J.; Dukes, M. J.; Kelly, D. F. *Nanoscale* **2021**, *13*, 7285−7293.

(21) Sun, Y.; Ge, L.; Udhane, S. S.; Langenheim, J. F.; Rau, M. J.; Patton, M. D.; Gallan, A. J.; Felix, J. C.; Rui, H. *Methods Protoc.* **2021**, *4*, 47.

(22) Li, T.; Wang, L.; Wang, H.; Li, X.; Zhang, S.; Xu, Y.; Wei, W. *Front. Cell. Infect. Microbiol.* **2020**, *10*, 470.

(23) Shan, D.; Johnson, J. M.; Fernandes, S. C.; Suib, H.; Hwang, S.; Wuelfing, D.; Mendes, M.; Holdridge, M.; Burke, E. M.; Beauregard, K.; Zhang, Y.; Cleary, M.; Xu, S.; Yao, X.; Patel, P. P.; Plavina, T.; Wilson, D. H.; Chang, L.; Kaiser, K. M.; Nattermann, J.; Schmidt, S. V.; Latz, E.; Hrusovsky, K.; Mattoon, D.; Ball, A. J. *Nat. Commun.* **2021**, *12*, 1931.

(24) Oliveira, S. C.; de Magalhães, M. T. Q.; Homan, E. J. *Front. Immunol.* **2020**, *11*, 587615.

(25) Anderson, G. P.; Liu, J. L.; Esparza, T. J.; Voelker, B. T.; Hofmann, E. R.; Goldman, E. R. *Anal. Chem.* **2021**, *93*, 7283−7291.

(26) Chen, Z.; Wu, Q.; Chen, J.; Ni, X.; Dai, J. *Virol. Sin.* **2020**, *35*, 351−354.

(27) Liu, R.; He, L.; Hu, Y.; Luo, Z.; Zhang, J. *Chem. Sci.* **2020**, *11*, 12157−12164.

(28) Zhang, L.; Fang, X.; Liu, X.; Ou, H.; Zhang, H.; Wang, J.; Li, Q.; Cheng, H.; Zhang, W.; Luo, Z. *Chem. Commun.* **2020**, *56*, 10235−10238.

(29) Zhang, J.; Oueslati, R.; Cheng, C.; Zhao, L.; Chen, J.; Almeida, R.; Wu, J. *Biosens. Bioelectron.* **2018**, *112*, 48−53.

(30) Li, J.; Lillehoj, P. B. *ACS Sensors* **2021**, *6*, 1270−1278.

(31) Hodge, C. D.; Rosenberg, D. J.; Grob, P.; Wilamowski, M.; Joachimiak, A.; Hura, G. L.; Hammel, M. *mAbs* **2021**, *13*, 1905978.

(32) Yamaoka, Y.; Miyakawa, K.; Jeremiah, S. S.; Funabashi, R.; Okudela, K.; Kikuchi, S.; Katada, J.; Wada, A.; Takei, T.; Nishi, M.; Shimizu, K.; Ozawa, H.; Usuku, S.; Kawakami, C.; Tanaka, N.; Morita, T.; Hayashi, H.; Mitsui, H.; Suzuki, K.; Aizawa, D.; Yoshimura, Y.; Miyazaki, T.; Yamazaki, E.; Suzuki, T.; Kimura, H.; Shimizu, H.; Okabe, N.; Hasegawa, H.; Ryo, A. *Cell Rep. Med.* **2021**, *2*, 100311.

(33) Tian, J.; Liang, Z.; Hu, O.; He, Q.; Sun, D.; Chen, Z.; Oueslati, R.; Cheng, C.; Wu, J.; Chen, J. *Electrochim. Acta* **2021**, *387*, 138553.

(34) Oueslati, R.; Cheng, C.; Wu, J.; Chen, J. *Biosens. Bioelectron.* **2018**, *108*, 103−108.

(35) Li, S.; Cui, H.; Yuan, Q.; Wu, J.; Wadhwa, A.; Eda, S.; Jiang, H. *Biosens. Bioelectron.* **2014**, *51*, 437−443.

(36) Mirzajani, H.; Cheng, C.; Wu, J.; Chen, J.; Eda, S.; Najafi Aghdam, E.; Badri Ghavifekr, H. *Biosens. Bioelectron.* **2017**, *89*, 1059−1067.

(37) Zhang, J.; Fang, X.; Mao, Y.; Qi, H.; Wu, J.; Liu, X.; You, F.; Zhao, W.; Chen, Y.; Zheng, L. *NPJ Sci. Food* **2021**, *5*, 12.

(38) Qi, H.; Wang, B.; Liang, H.; Wu, J. J.; Ni, T.; Huang, Z.; Lu, Y.; Zhang, J. *IEEE Sens. J.* **2021**, *21*, 755−764.

(39) Wu, J. *IET Nanobiotechnol.* **2008**, *2*, 14−27.

(40) Salari, A.; Thompson, M. *Sens. Actuators, B* **2018**, *255*, 3601−3615.

(41) Liu, X.; Cheng, C.; Wu, J.; Eda, S.; Guo, Y. *Biosens. Bioelectron.* **2017**, *90*, 83−90.

(42) Yang, K.; Islam, N.; Eda, S.; Wu, J. *Microfluid. Nanofluid.* **2017**, *21*, 35.

(43) Cheng, C.; Wu, J.; Fikrig, E.; Wang, P.; Chen, J.; Eda, S.; Terry, P. *ChemElectroChem* **2017**, *4*, 485−489.

(44) Zhang, J.; Fang, X.; Wu, J.; Hu, Z.; Jiang, Y.; Qi, H.; Zheng, L.; Xuan, X. *Biosens. Bioelectron.* **2020**, *150*, 111879.

(45) Zhang, J.; Zhang, Y.; Wu, J.; Qi, H.; Zhao, M.; Yi, M.; Li, Z.; Zheng, L. *Sens. Actuators, B* **2021**, *329*, 129282.